Ozone Tagging Velocimetry Using Narrowband Excimer Lasers

Lubomir A. Ribarov,* Joseph A. Wehrmeyer,† Farrokh Batliwala,‡ and Robert W. Pitz§
Vanderbilt University, Nashville, Tennessee 37235-1592
and
Peter A. DeBarber¶
MetroLaser, Inc., Irvine, California 92614-6428

Ozone tagging velocimetry (OTV), a nonintrusive, unseeded, time-of-flight velocity measurement technique, consists of a write step, where a 193-nm pulsed excimer laser creates an O_3 line via O_2 uv absorption, and a subsequent read step, where a 248-nm excimer laser photodissociates the O_3 and fluoresces the vibrationally excited O_2 product, revealing the tag line displacement. For the first time, instantaneous OTV images and velocity measurements are reported in airflows at room temperature. The narrowband lasers are tuned to the O_2 Schumann–Runge transitions improving the OTV signal strength by a factor of six over that obtained using two broadband lasers. This improvement is less than expected from absorption ratio estimates, due in part to incomplete laser locking efficiency and possibly to laser bleaching. Diffusion of the O_3 tag line is shown to be important only for write–read delay times of the order of milliseconds or greater. Modeling of O_3 concentration vs time shows O_3 is long lived at room temperature and relatively insensitive to water vapor, but O_3 peak concentration and lifetime greatly decrease at high temperature, though high pressure increases peak O_3 concentration.

Introduction

ALTHOUGH species concentrations and temperature are routinely measured by laser–molecular interactions (laser-induced fluorescence, Raman scattering), velocity is most often measured by the introduction of foreign seed particles, such as oil droplets or ceramic particles. Particle-imaging velocimetry systems are commercially available and provide velocity field measurements based on time-of-flight data from many particles. However, seeding non-uniformities and particle drag can lead to differences between the particle and gas velocity fields. Other issues related to environmental and operational concerns often discourage the introduction of particles into large wind-tunnel test facilities. Velocity measurement techniques have been developed where the flow is seeded with a molecular tracer, i.e., iodine, biacetyl, nitric oxide, or sodium, rather than particles. Many of these tracers are either corrosive or toxic.

There remains a need for an optically based molecular velocity field measurement technique that is unseeded. A flow tracer or tag should be created, photochemically or otherwise, from the ambient gas species to obviate seeding requirements. High-speed (supersonic) unseeded air velocity fields have been measured using the Doppler shift of Rayleigh scattering.[1] For lower speeds though, direct Doppler methods are not as accurate as time-of-flight methods. Several time-of-flight molecular flow tagging velocity measurement techniques have been developed that do not require seeding. Most of these techniques create a tag by nonlinear optical processes that limit the length of the tagged line to a few millimeters. For example, using two-photon photodissociation of water vapor, a tag line of the hydroxyl radical (OH) can be created and subsequently made to fluoresce to pr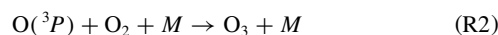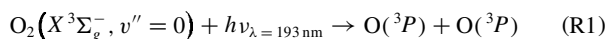ofile flow velocity.[2] In the RELIEF method, a nonlinear stimulated Raman process produces a tag line of vibrationally excited oxygen (O_2) whose enhanced fluorescence strength reveals the displacement of the tag when the flowfield is subsequently irradiated by an ultraviolet laser.[3] The short lifetime of vibrationally excited O_2, especially in water-laden air, generally limits RELIEF to high-speed, dry flows. Thus, there is still a need for an unseeded molecular flow tagging technique that is amenable to low- or high-speed flows of either dry or humid air.

This paper describes a technique being developed to fill that need: instantaneous ozone tagging velocimetry (OTV).[4] Ozone (O_3), produced from O_2, is the flow tag and is relatively long lived and insensitive to water vapor's presence. It is produced and detected via single-photon processes, which allow the use of long tag lines. Tag lines of 40-mm length are used in an instantaneous OTV flow profile presented in this paper. Several OTV developmental issues are also investigated, including the dependence of O_3 production on temperature, and the relative merit of using narrowband or broadband lasers.

OTV Photochemistry

Figure 1 shows a conceptual drawing of the OTV technique. First a tag line of O_3 is created from O_2 by a pulsed argon–fluoride (ArF) excimer laser operating at ∼193 nm. After a known delay time, the O_3 tag line position is revealed through O_3 photodissociation and subsequent O_2 fluorescence, both caused by a pulsed laser sheet from a krypton–fluoride (KrF) excimer laser operating at ∼248 nm. A digital camera images the fluorescence from the initial and final line locations; thus, a means for establishing a velocity profile is provided.

The following two reactions are involved in photochemically writing the O_3 line:

$$O_2\left(X\,^3\Sigma_g^-, v'' = 0\right) + h\nu_{\lambda = 193\,\text{nm}} \rightarrow O(^3P) + O(^3P) \qquad (\text{R1})$$

$$O(^3P) + O_2 + M \rightarrow O_3 + M \qquad (\text{R2})$$

In reaction (R1), O_2 in the ground ($X\,^3\Sigma_g^-$) electronic and ground vibrational ($v'' = 0$) state absorbs a single photon of 193-nm light and decomposes into ground state (^3P) O atoms, due to the excited molecular state's ($B\,^3\Sigma_u^-$) high predissociation rate. The ArF laser accesses the (4 ← 0) vibrational transition in the Schumann–Runge band, and typical values of predissociation linewidth are 3 cm^{-1} for this transition,[5] indicating a predissociation rate of the order of 10^{11} s^{-1}. This is the highest predissociation rate of any of the Schumann–Runge vibrational transitions, which partially compensates for the relatively low Franck–Condon factor of the (4 ← 0)

1. "WRITING" **2. "READING"**

tagged line
written with 193 nm pulse
at t_0

displaced line
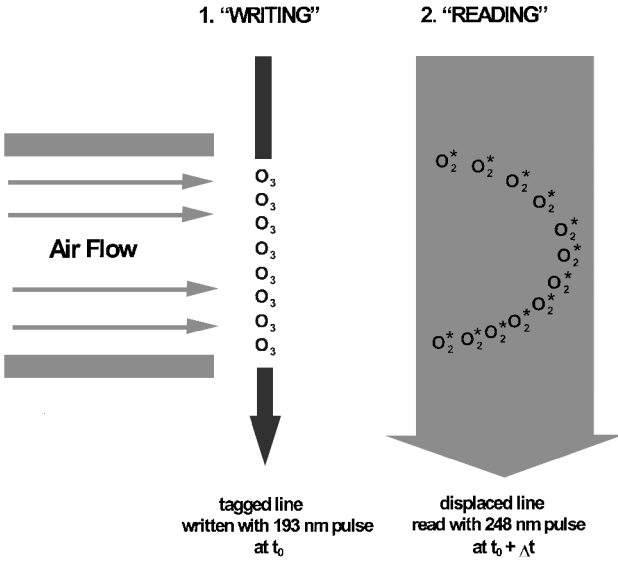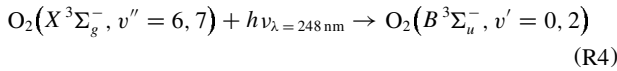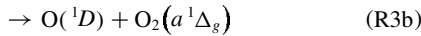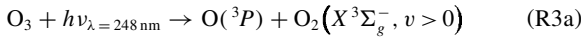read with 248 nm pulse
at $t_0 + \Delta t$

Fig. 1 OTV conceptual schematic.

transition compared to those originating in vibrationally excited levels.[6] In reaction (R2) the atomic oxygen produced by photodissociation combines with O_2, via a three-body reaction with an inert M, to form O_3. The reaction rate coefficient k_2 for reaction (R2) governs this O_3 production. For $M = N_2$, $k_2 = 5.7 \times 10^{-46}$ m^6/s at standard conditions and is approximately the same if $M = O_2$ (Ref. 7). The growth time of O_3 (to $\sim$63% of steady-state concentration) for standard conditions is then $1/(k_2 n_{O_2} n_{N_2}) \cong 20\,\mu$s, where n is number density.

The displaced O_3 line is read by the 248-nm light sheet through reactions (R3a) and (R4)

$$O_3 + h\nu_{\lambda = 248\,nm} \rightarrow O(^3P) + O_2\left(X\,^3\Sigma_g^-, v > 0\right) \qquad (R3a)$$

$$\rightarrow O(^1D) + O_2\left(a\,^1\Delta_g\right) \qquad (R3b)$$

$$O_2\left(X\,^3\Sigma_g^-, v'' = 6, 7\right) + h\nu_{\lambda = 248\,nm} \rightarrow O_2\left(B\,^3\Sigma_u^-, v' = 0, 2\right) \qquad (R4)$$

The KrF laser's 248-nm wavelength output efficiently dissociates O_3 because the broad peak of the O_3 Hartley absorption band, the strongest of the O_3 bands, occurs from about 245 to 265 nm (Ref. 8). In fact, with an absorption cross section of approximately 10^{-17} cm^2 per molecule, and 248 nm fluences of the order of 40 J/cm^2, it is expected that all of the O_3 will be photodissociated by a single laser pulse. However, in the earlier work,[4] multiple reads of an ozone ribbon were accomplished.

Two photodissociation paths exist for O_3 after uv absorption: decomposition to a ground state O atom and vibrationally excited O_2 as shown in reaction (R3a) or to electronically excited O and O_2 as shown in reaction (R3b). The fraction of photodissociating O_3 that decomposes via path (R3a) has been estimated to be from 0.06 to 0.15 for 248-nm excitation.[9] The O_2 molecules formed by this path are widely distributed among the ground electronic state's vibrational levels, with a maximum population fraction occurring for $v'' = 8$, but with only slightly lower population fractions occurring for $v'' = 6$ or 7 (Ref. 10). These two vibrational levels can result in fluorescence via Schumann–Runge transitions that are within the output range of the KrF laser. Specifically several rotational lines in the $(X\,^3\Sigma_g^- - B\,^3\Sigma_u^-, v'' = 6, 7$ to $v' = 0, 2)$ bands are accessible.[11] The $v' = 0, 2$ levels also have significant predissociation rates, though the rate for $v' = 0$ is about one-fourth that for $v' = 2$, which is itself lower than the $v' = 4$ rate by an order of magnitude.[5,12] Although the lower predissociation rate for the $(0 \leftarrow 6)$ transition compared to the $(2 \leftarrow 7)$ indicates it may be the better transition for fluorescence production, the relative strength of the two excitation transitions also must be considered, with the $(2 \leftarrow 7)$ having about a factor of 30 higher Franck–Condon factor than the $(0 \leftarrow 6)$. The fluorescence production from the two

excited levels also depends on the Franck–Condon factors of the fluorescence emission transitions, with the $(0 \rightarrow v'' > 6)$ transitions as a group having a larger average Franck–Condon factor than the $(2 \rightarrow v'' > 7)$ transitions. Another issue associated with the choice of $(0 \leftarrow 6)$ or $(2 \leftarrow 7)$ pumping is the filtering scheme used to suppress detected 248-nm scattering because the strongest emission lines from $(2 \rightarrow 7)$ excitation are closer to 248 nm than the strongest emission lines from $(0 \rightarrow 6)$ pumping.[11,13] Experimentally, it is determined that pumping the $(0 \leftarrow 6)$ vibrational transition is the most efficient in terms of producing detectable fluorescence.

One concern for OTV is its applicability to high-temperature and/or high-pressure flowfields, such as the internal and exhaust flows of gas turbine engines. Whereas the half-life of dilute O_3 is of the order of hours at standard conditions,[14] it quickly diminishes with increasing temperature. Another issue is the effect of minor air species on O_3 concentration, i.e., water vapor in open-circuit wind tunnels that simulate sea-level conditions and nitric oxide (NO) present in gas turbine exhausts. To predict the concentration of O_3 as a function of temperature, pressure, and time, the Chemkin II thermodynamic database and the SENKIN[15] chemical kinetics solver are used with a set of 119 reversible reactions, including reactions involving nitrogen oxides.[16]

Figure 2 shows a plot of O_3 concentration as a function of time in three different environments: dry air, humid air, and polluted humid air. In the case of dry air, the initial mole fractions of N_2, and O_2 are 79.00% and 20.79% respectively. This calculation assumes $\sim$1% of the O_2 molecules are photodissociated into O atoms by the ArF laser. This percentage is typical of broadband ArF laser excitation (average absorption coefficient estimated at 0.01 cm^{-1} across the laser bandwidth)[17] with approximately 100 mJ delivered into a 0.5-mm-diam circular area (fluence of 50 J/cm^2).

For dry air at standard conditions, with an estimated initial atomic oxygen concentration of 4200 ppm (1% dissociation of ambient O_2), a steady-state O_3 concentration of $\sim$3300 ppm is predicted to occur after $\sim$1 ms. This value is slightly lower than previous predictions[4] because of improvements in the reaction rate estimates. Figure 2 also shows that within 20 μs the O_3 concentration has attained over 50% of it steady-state value, as predicted from analysis of reaction (R2) only. For the other two cases shown in Fig. 2, the steady-state O_3 concentrations are lower. The slight drop in steady-state O_3 concentration for the humid air is due to an initially lower O_2 concentration and, hence, O atom concentration (still assuming 1% dissociation). The addition of 3.5% mole fraction of water vapor has no appreciable chemical effect on O_3 concentration. Polluted humid air is modeled with an addition of 100 ppm of NO to the humid air. The presence of NO efficiently removes O_3 by following well-known reaction, important in tropospheric pollution modeling[8]:

$$NO + O_3 \rightarrow NO_2 + O_2 \qquad (R5)$$

The presence of NO also acts to inhibit O_3 production by scavenging O according to

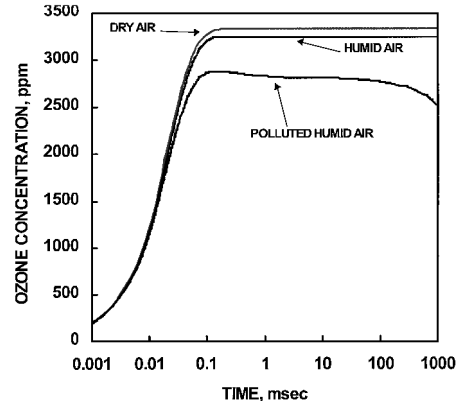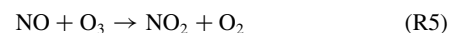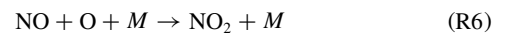$$NO + O + M \rightarrow NO_2 + M \qquad (R6)$$

Fig. 2 O_3 concentration vs time for dry air, humid air, and polluted humid air with 100 ppm NO: all cases at 1-atm constant pressure, 300-K initial temperature, and assuming initial 1% dissociation of ambient O_2.
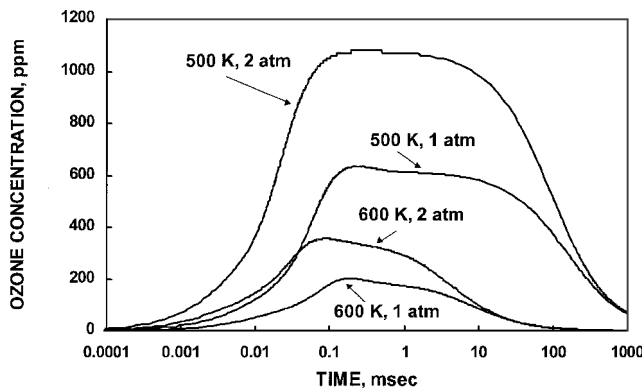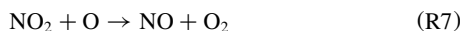
Fig. 3 O_3 concentration vs time for dry air for several constant pressure and initial temperature combinations: all cases assume initial 1% dissociation of ambient O_2.

$$NO_2 + O \rightarrow NO + O_2 \qquad (R7)$$

The results of Fig. 2 are all for an initial temperature of 300 K, and a slight temperature rise (typically ∼30 K) occurs as a result of the initial laser absorption that dissociates O_2 and subsequent heat release in O_3 formation from O and O_2 (Refs. 4 and 16).

As initial temperature is increased, O_3 reactions associated with the thermal decomposition of O_3 become important at limiting both the maximum amount of O_3 formed and the length of time that a significant O_3 concentration exists. Ozone thermal decomposition generally involves two-body collisions of the form

$$M + O_3 \rightarrow M + O_2 + O \qquad (R8a)$$

$$O + O_3 \rightarrow 2O_2 \qquad (R8b)$$
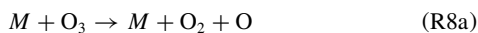
where M is any major species, all having similar reaction efficiencies.[18] It is known that reducing the temperature of stored gaseous ozone by only a few degrees from standard temperature can greatly increase its thermal decomposition half-life,[14] and likewise, raising its temperature can reduce the O_3 lifetime. This is shown in Fig. 3, where dry air with an initial O atom concentration of 4200 ppm (1% dissociation of ambient O_2) is subjected to various pressure and initial temperature conditions. For an initial temperature of 500 K and a constant pressure of 1 atm, the peak O_3 concentration is lowered to 600 ppm, down from the 3300 ppm peak value for the 300-K initial condition. The lifetime of O_3 is greatly reduced at high-temperature conditions with O_3 disappearing almost entirely in 1 s. These traits of reduced peak concentration and lifetime are even more pronounced when the initial temperature is increased to 600 K. The peak O_3 concentration falls to 200 ppm, and O_3 almost completely disappears within 100 ms. The reduced O_3 lifetime is not a serious issue in the application of OTV to elevated temperature flows because delay times between write and read laser pulses typically range from 20 μs to 2 ms for medium-to-high speed flows. However, the concomitant drop in peak O_3 concentration is problematic because the read laser produces less fluorescence signal as a result of the lower O_3 and vibrationally excited O_2 populations.

Figure 4 shows peak O_3 concentration as a function of temperature for dry air at 1 atm. The peak concentration can be seen to drop almost linearly with temperature down to about 200 ppm at 600 K, where it continues to drop, though at a slower rate, with increasing temperature. Whereas these predictions indicate the inapplicability of OTV to high-temperature, atmospheric pressure flows, it may still be applicable to flows at both high temperature and pressure, such as compressor flowfields. Because the O_3 production path involves a trimolecular reaction (R2) while the destruction path involves bimolecular collisions (R8a) and (R8b), the O_3 production rate relative to the destruction rate will be enhanced with an increase in pressure. This is shown in Fig. 3, where increased peak O_3 concentrations occur when the pressure is increased from 1 to 2 atm. For both initial temperature conditions, the peak O_3 concentration is almost doubled by doubling the pressure.
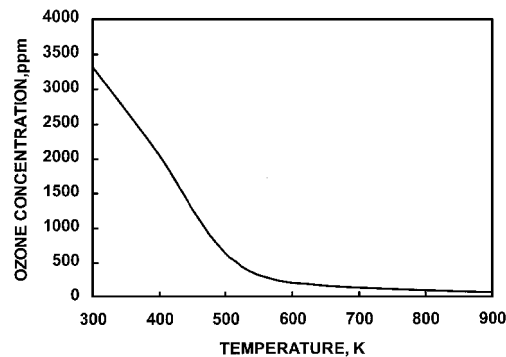

Fig. 4 Peak O_3 concentration vs initial temperature for dry air at 1 atm, assuming initial 1% dissociation of ambient O_2.
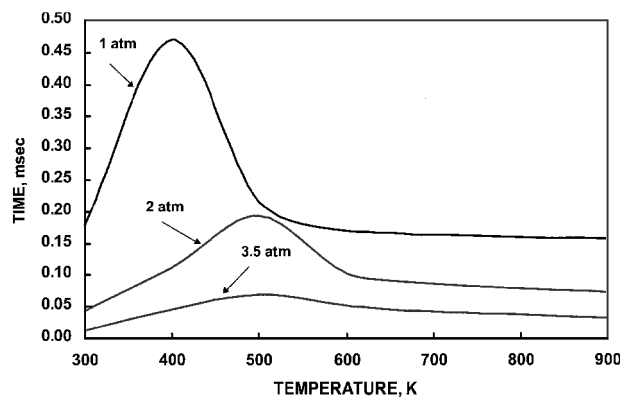

Fig. 5 Time required to achieve 99% of peak O_3 concentration vs initial temperature for dry air, assuming initial 1% dissociation of ambient O_2.

In addition to influencing the peak O_3 concentration, the temperature and pressure conditions of the tagged flowfield also affect the time at which the peak concentration occurs. The optimum time delay should be some time shorter than the time at which significant O_3 is destroyed, and yet long enough to ensure irradiation of nearly the maximum concentration of O_3. Figure 5 shows the time required, as a function of temperature, to produce 99% of the peak O_3 concentration for dry air at three pressures. At 1 atm, the time for peak O_3 concentration varies between 200 and 450 μs as temperature is increased. At higher pressures the time for peak O_3 is reduced, ranging from 50 to 200 μs for 2 atm and from 10 to 50 μs for 3.5 atm.

Narrowband/Broadband Experimental Comparison

Time-averaged OTV images have previously been demonstrated in air using broadband ArF and KrF lasers.[4] Two narrowband lasers, whose output can be tuned onto specific O_2 transitions to maximize either photodissociation or fluorescence yields, are expected to enhance OTV signal strength over that obtained from broadband lasers and allow instantaneous OTV imaging.

In the present work, two Lambda-Physik lasers are used: a COMPex-150T (∼0.003-nm linewidth tunable from 192.9 to 193.9 nm) and an EMG-160T MSC (∼0.001-nm linewidth tunable from 248 to 249 nm). In addition to narrowband operation, both lasers can be operated in the broadband mode with output linewidths equal to their tuning ranges. Figure 6 shows a schematic of the OTV system. The output from the ArF laser is focused to a beam waist of approximately 0.5 mm using a 1-m focal length lens. Several of the following OTV images use only one focused ArF beam whereas others use a pair of crossed beams with the second beam formed using a 50% beamsplitter inserted into the system, as shown in Fig. 6. Total travel length for the ArF beams is from 1.5 to 2 m. The KrF beam is focused to a sheet using a 1-m focal length cylindrical lens, providing a sheet with a 2 cm by 0.5 mm cross section. A Nikon uv camera lens and a Princeton Instruments imaging charge-coupled device camera comprise the light detection system. Two different filter combinations are used for the follow-

ing OTV images. One combination uses two identical interference filters in series (Laseroptik GmbH, 0-deg incidence notch filters) to block 248-nm Rayleigh scattering. Even though the camera intensifier is gated only during the KrF laser firing, this filter scheme allows 193-nm Rayleigh scattering to mark the original tag line location, due to photocathode image persistence. A second filter combination is also used, consisting of only one 248-nm notch interference filter in series with a 10-mm-thick liquid butyl acetate filter. The liquid filter acts as a long-pass filter to block all light shorter than ~253 nm, and thus, the 193-nm Rayleigh scattering is also attenuated.

Figure 7 shows four time-averaged (20 laser pulse pairs) OTV images obtained in a uniform airflow (~3 m/s) with each image for a specific combination of narrowband and/or broadband lasers. The nozzle producing the uniform flow is a 25-mm-diam Hencken burner with a 12.5-mm-diam core surrounded by an annular coflow region. The coflow was not used, so that a 12.5-mm uniform flowfield is provided. The time delay between write and read laser pulses is 4 ms. In narrowband operation the lasers are tuned to the following wavelengths: 193.293 nm, corresponding to the predissociation-broadened P(17) and R(19) $(4 \leftarrow 0)$ transitions, and 248.534 nm for the R(17) $(0 \leftarrow 6)$ transition. These four images were obtained using the two interference filters in series, and as a result, the original write line location can be seen under the displaced line location by the 193-nm Rayleigh scattering. Scattering off the 25-mm nozzle produced the dark images at the bottom. Strength of signal is greatly improved by using two narrowband lasers rather than two broadband lasers, as shown in Fig. 7 by the increased signal of the upper left OTV image compared to the lower right. Graphs of signal vs vertical position are shown to the left of each image. These graphs correspond to the slice indicated by the vertical arrows. Horizontal arrows show the OTV signal appearing in each graph. For single narrowband and single broadband laser operation, a narrowband ArF laser provides slightly better signal than a narrowband KrF laser. Signal to noise ratios for the four images are 39, 15, 6, and 19, clockwise from upper left, estimated by averages of displaced OTV line signal divided by background noise, mainly due to 248-nm scattering.

Improvement in signal going from broadband to narrowband operation can be estimated by considering the amount of light in the narrowband mode that is at wavelengths efficient for excitation compared to the amount in the broadband mode. For the ArF laser the improvement should then be approximately a factor of four, based on the absorption spectrum of 295 K air.[17] Because of the reduced predissociation linewidths of the $v' = 0$ transitions and the resulting sparseness in the absorption spectrum,[13] the expected improvement going from broadband to narrowband KrF laser operation should be even greater, estimated to be approximately a factor of 10. One reason that these estimated improvements are not fully realized in the images of Fig. 7 could be the incomplete locking efficiency of both of the narrowband lasers. Another possibility is the potential saturation of an excitation transition. This is more probable for the $(0 \leftarrow 6)$ transition, which involves a smaller O_2 population and has a Franck–Condon factor of 1.5×10^{-3}, almost three orders of magnitude higher than the 3×10^{-6} value for the $(4 \leftarrow 0)$ transition.[6]

Instantaneous OTV Velocity Profile

Figure 8 shows an instantaneous OTV image, obtained from a single laser pulse from each laser. Both lasers are operated in the narrowband mode. A straight nozzle, attached to a loudspeaker receiving a 1-Hz square wave signal, produces a cylindrically symmetric, mushroom-shaped vortical flowfield. Two tag lines, with the second line created using a 50% beamsplitter (as shown in Fig. 6), are used to provide a cross, whose center provides an unambiguous point to determine velocity. The cross center's 8-mm displacement during the 4-ms delay gives a measured velocity of 2 m/s. For this OTV image the butyl acetate liquid filter is used, greatly reducing detected 193-nm Rayleigh scattering. As a result, the original tag line position is not marked by light scatter in this image, though other OTV images with 0 ms read/write delays confirm the tag lines' initial locations, which are shown by the dashed lines in Fig. 8.

OTV Filter Selection

Figures 7 and 8 were obtained using two different filter combinations. A butyl acetate filter may be desirable if 193-nm light interferes with OTV signal detection, possibly when scattering surfaces
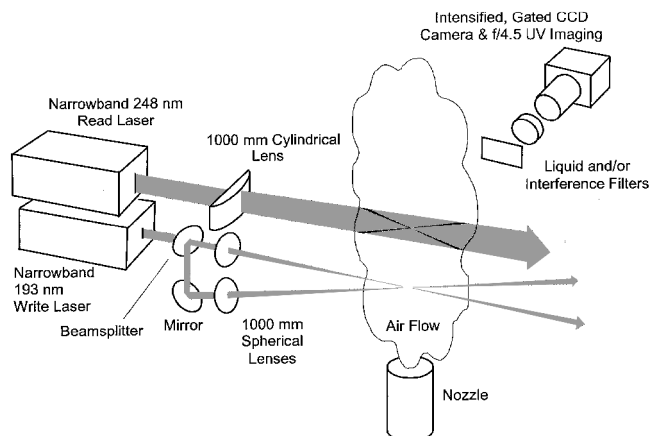
Fig. 6 OTV experimental setup using two narrowband excimer lasers and two write beams.
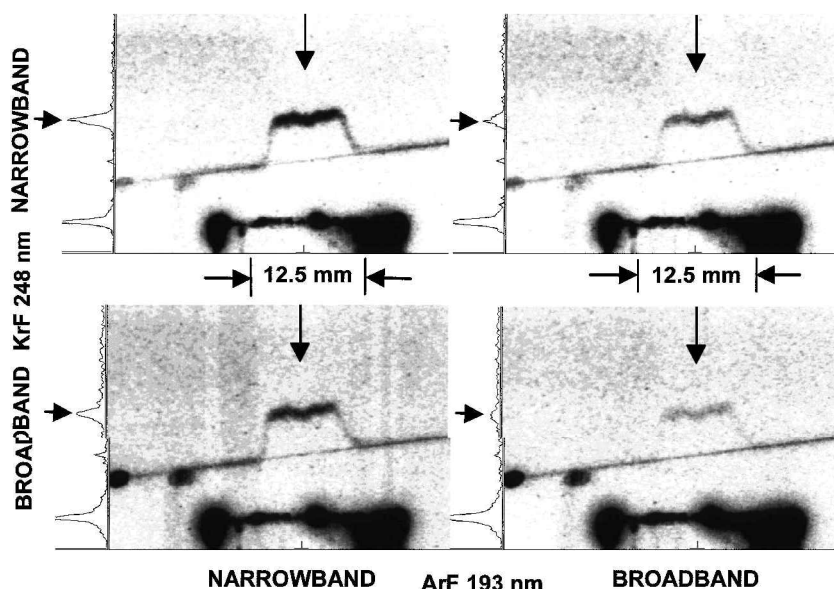
Fig. 7 Time-averaged OTV images, with 4-ms delay time, for 12.5-mm-diam uniform flowfield of room temperature dry air.
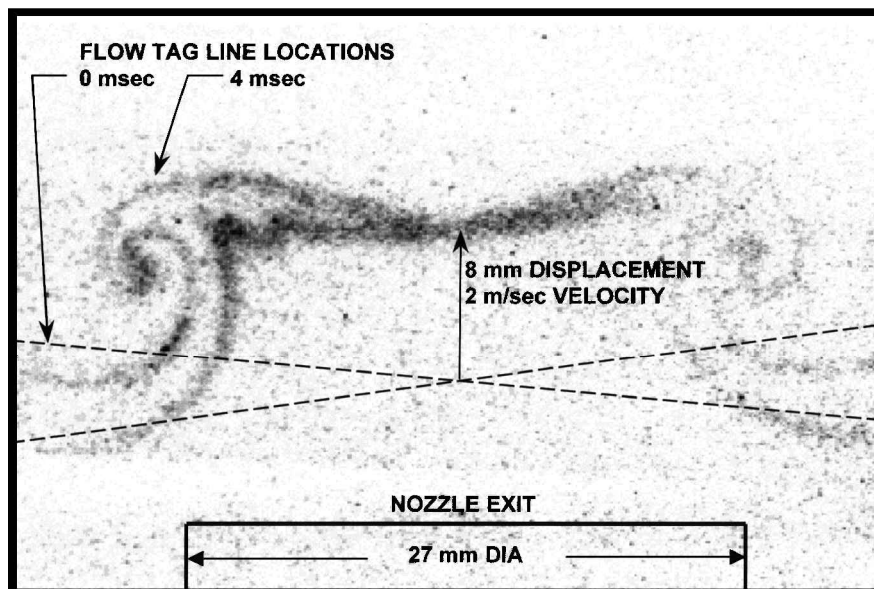
Fig. 8   Instantaneous OTV image of room temperature dry air flowfield; vortex created by nozzle attached to a loudspeaker receiving a 1-Hz square wave signal.
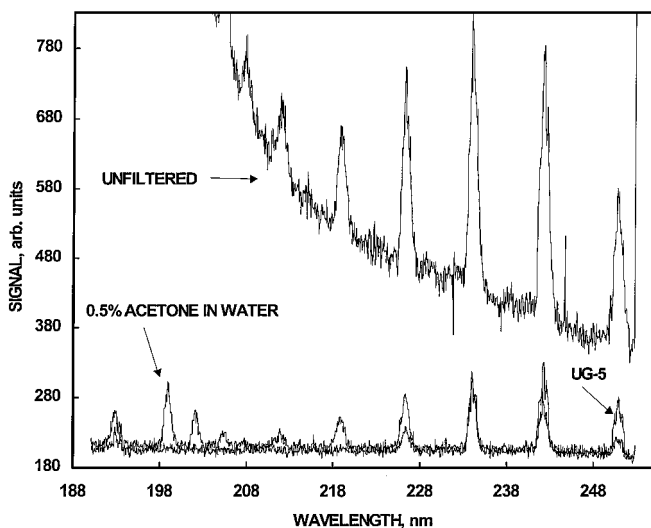

Fig. 9 O_2 fluorescence spectra from 193-nm narrowband ArF laser excitation tuned to O_2 transition; each spectrum associated with one detection filter condition: 1-mm-thick Schott UG-5 color glass filter, 10-mm-thick 0.5% acetone in water liquid filter, and unfiltered.

Fig. 10   Instantaneous OTV images for 12.5-mm-diam uniform flow-field of room temperature dry air.

are within the detection system field of view. However, other filter options exist that block both 193- and 248-nm light but allow fluorescence detection for O_2 transitions between these wavelengths. The O_2 laser-induced fluorescence spectra from $(4 \leftarrow 0)$ 193-nm excitation is shown in Fig. 9 for various filter combinations. Figure 9 shows that a liquid acetone filter[19] (10-mm thick, 0.5% acetone in water solution) or a 1-mm-thick Schott UG-5 filter both greatly attenuate 193-nm light while allowing through longer wavelength O_2 fluorescence. Whereas the acetone filter is more transmissive from 198 to 228 nm, the glass filter becomes the more transmissive at longer wavelengths. Combinations of these 193-nm filters and the 248-nm interference notch filters can be used when a background of intense scattered light is present at both wavelengths.

Effect of Molecular Diffusion on OTV Velocity Measurement

As the delay time between read and write steps, Δt, is increased, the displacement of the O_3 line from its original position, Δx, also increases. In addition, the width of the O_3 tag line, ω, increases due to molecular diffusion. The increase in ω with Δt can affect velocity
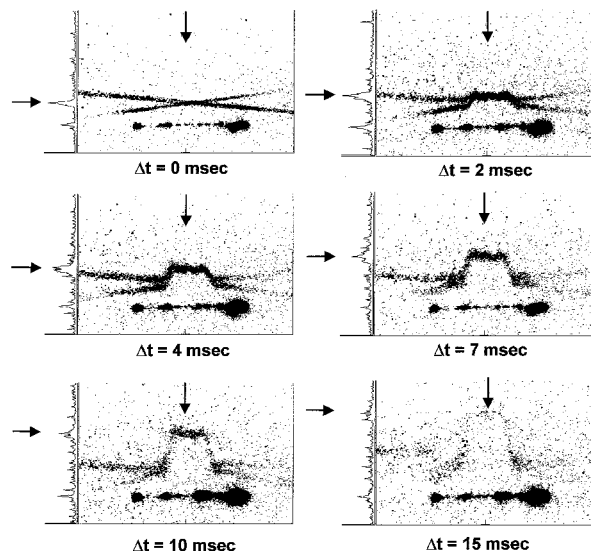
measurement accuracy by increasing the error in a measurement of Δx.

For the instantaneous OTV images shown in Fig. 10, the Hencken burner is again used to produce a uniform flowfield over an approximately 12-mm-diam circular area. The ArF write beam remains split into two beams to form a cross. Each of the six OTV images in Fig. 10 are for a specific Δt, ranging from 0 to 15 ms. Graphs of signal strength, shown to the left of each image, correspond to locations shown by vertical arrows. Horizontal arrows point to OTV signal. As Δt is increased, molecular diffusion causes the tag lines to widen and the peak OTV fluorescence signal to diminish due to the reduced local concentration of O_3. Values of experimentally measured ω range from an initial width ω_0 of 500 μm at $\Delta t = 0$ ms, up to $\omega = 1600$ mm for $\Delta t = 15$ ms. This can be compared to an expected value of ω using the following theoretical relationship, valid for an initial Gaussian distribution of O_3 concentration across ω_0 (Ref. 20):

$$\omega = \left[8 \, ln(2)\Delta t \, D + \omega_0^2\right]^{\frac{1}{2}} \quad (1)$$

where D is the diffusion coefficient of O_3 into air. By the approximating of D as the binary diffusion coefficient of O_3 into N_2 and
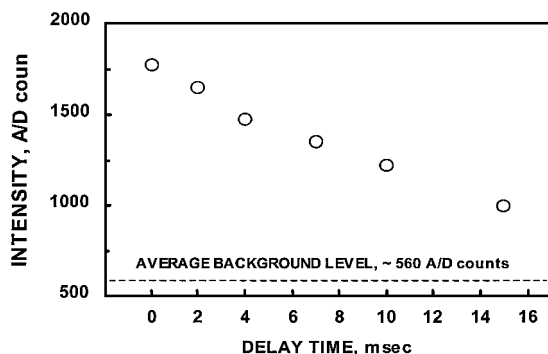
Fig. 11 Instantaneous OTV signal vs delay time Δt between write and read laser pulses.

the using of critical thermodynamic properties for those two gases, D is estimated as 0.15 cm^2/s at standard conditions. A calculated ω of 1200 μm is obtained for $\Delta t = 15$ μs, about 25% less than the measured value. This difference could be caused by local heating along the tag line from photolytic processes, including O$_3$ formation, resulting in increased molecular diffusion.

The uncertainties ($\sigma_{\Delta x}$, $\sigma_{\Delta t}$) in the measurements of Δx and Δt affect the overall velocity measurement uncertainty σ_V. However, σ_V is dominated by $\sigma_{\Delta x}$ because Δt is accurately controlled using a digital delay generator with picosecond resolution, and the timing jitter of each laser is specified at only ± 2 ns. If it is assumed that $\sigma_{\Delta x}$ depends only on identifying the center of the displaced tag line within its width ω (with the center of ω_0 accurately known), and if 10% of ω is assumed as the uncertainty in identifying its center, then the ratio of σ_V to measured velocity V can be estimated as

$$\sigma_V/V \cong \sigma_{\Delta x}/\Delta x \cong 0.1\omega/\Delta x = 0.1\omega/(\Delta t\, V) \qquad (2)$$

For instance, by the assumption of values of ω of 1 mm and $\Delta x \approx 10\omega \cong 10$ mm (a situation similar to that of Fig. 8), the relative uncertainty in displacement measurement, and, hence, in velocity measurement, is ~1%.

At standard conditions, a tagged line with $\omega_0 = 0.5$ mm requires ~5 ms to double its width due to diffusion. Thus, for short time delays and fast velocities, e.g., $\Delta t < 1$ ms and $V > 5$ m/s, molecular diffusion effects become negligible for 1% accurate velocity measurements as ω remains essentially ω_0 during the short Δt. For example, at 5 m/s, a 0.5-mm line will displace 5 mm in 1 ms making a 1% measurement possible if the line center can be located to 10% of its width. The 20-μs formation time of O$_3$ acts as a lower limit on Δt as significant reductions in OTV signal occur at $\Delta t < 20$ μs, resulting in increased uncertainty at locating the displaced OTV line.

Examination of Eqs. (1) and (2) suggests that, to reduce σ_V/V, the value of Δt should be as large as practicable, given the imaging system dimensions because Δx scales with Δt whereas ω scales only with the square root of Δt. However, at large Δt, the uncertainty in determining the line center of ω increases above 0.1ω due to diffusion and resultant reduced OTV fluorescence signal. Figure 11 shows the measured OTV signal strength as a function of Δt, with data taken from the images of Fig. 10 at locations shown by the crossings of the horizontal and vertical arrows in Fig. 10. Also shown in Fig. 11 is the average background level (~560 A/D counts) for the images of Fig. 10. As Δt is increased from 0 to 15 ms, the OTV signal drops from ~1750 counts down to ~1000 counts, both including background. Thus, the contrast ratio drops by almost a factor of two, and the presence of the OTV line, as well the location of its line center, becomes increasingly hard to detect.

Conclusions

OTV, previously demonstrated only as a time-averaging velocity measurement method,[4] has been shown as capable of providing instantaneous velocity measurements in room temperature airflows. Tag line lengths over 40 mm in length are imaged instantaneously. This is possible because the single-photon processes of both the write and read steps are insensitive to beam focus, thus allowing long tag lines to be created with equal strength down the write line and to be imaged with equal efficiency down the read sheet.

One of the main reasons for the current improvement from time-averaged to instantaneous OTV imaging is the additional signal obtainable using narrowband uv excimer lasers, rather than broadband versions. It is demonstrated that by tuning the narrowband lasers onto specific O$_2$ Schumann–Runge transitions, the resulting OTV signal strength is markedly improved, by a factor of six, over a system using two broadband lasers. The signal increase is less than expected based on ratios of estimated absorption coefficients for narrowband or broadband operation. The discrepancy is at least partly due to incomplete locking efficiency of the two narrowband lasers and possibly to bleaching of the excited state O$_2$ molecules involved in the read step.

For low velocities (<5 m/s) or long delay times (>1 ms), the diffusion of the displaced OTV tag line has been shown to be an important factor associated with the uncertainty in measuring the displacement of the OTV line. For delay times between the write and read pulses greater than ~15 ms, detection of the displaced OTV line and its line center becomes problematic. However, this should be an issue only when OTV is applied to very low-velocity flows, because typical delay times associated with medium- and high-velocity flows are much shorter, of the order of tens to hundreds of microseconds.

Improvements to the OTV system involve both increasing OTV signal and reducing background light. Improving the locking efficiency of both lasers can improve OTV signal by putting more of the available light energy into the most efficient wavelengths for O$_2$ excitation. When in narrowband operation, approximately 50% of the laser energy exiting the ArF is lost over a 1.5-m distance. Enclosing and purging the light path of O$_2$ between laser and sample volume will reduce this absorption problem. For the present work this purging was not done, nor was it performed inside of the ArF laser. By the purging of the O$_2$ from the light path in the laser, both the locking efficiency and the output energy of the ArF laser are expected to improve. Filter improvements can act to both increase OTV signal, by allowing in more O$_2$ fluorescence bands, and to reduce background, by more effectively blocking the 193- and 248-nm scattering. A combination of the 193-nm long-pass and 248-nm notch filters may be the best filter combination in terms of O$_2$ fluorescence transmission and Rayleigh/Mie scattering blocking. However, other scattering processes, most notably O$_2$ and N$_2$ Raman from 248-nm excitation, may dominate the background after the 193- and 248-nm wavelengths are effectively blocked. An effective filtering scheme could be to use a wide notch interference filter that blocks 264-nm N$_2$ Raman scattering as well as 248-nm scattering.

The numerical modeling of the O$_3$ formation chemistry shows O$_3$ to be a long-lived molecular tag in low-temperature flows of dry or humid air, even when the flowfield contains a significant amount of NO. However, as temperature increases, O$_3$ begins to thermally decompose soon after formation, with the peak concentration dropping from 3300 to 600 ppm, going from 300 to 500 K at a constant pressure of 1 atm. At temperatures above ~600 K, only trace amounts of O$_3$ are present even at times of peak concentration. An increase in pressure increases the peak O$_3$ concentration, by enhancing the rate of three-body O$_3$ formation reactions relative to two-body destruction reactions, with the increase in peak concentration scaling approximately as the increase in pressure. However, the reduction in O$_3$ concentration at high temperatures is significant enough that application of OTV to fully map the flowfields encountered in, for example, the exhausts of gas turbine engines or in lean–premixed combustors, will be problematic. Other types of unseeded molecular flow tags amenable to hot flows are currently being considered to act as a complementary hot tag to the cold O$_3$ tag. These tags would be complementary in the sense that one write laser can produce both tags along its path, with the O$_3$ tag produced in cold regions of the flowfield and the hot tag produced in the remaining hot regions. Both tags would also be operated on by the same read laser, revealing tag line displacements across the entire flowfield. This complementary hot/cold flow tag scheme is especially applicable to chemically reacting flowfields, such as those found in gas turbine combustors, where cold unreacted regions can coexist close to reacting or fully reacted hot regions.

Acknowledgments

References

[1]Forkey, J. N., Finkelstein, N. D., Lempert, W. R., and Miles, R. B., "Demonstration and Characterization of Filtered Rayleigh Scattering for Planar Velocity Measurements," *AIAA Journal*, Vol. 34, No. 3, 1996, pp. 442–448.

[2]Boedeker, L. R., "Velocity Measurement by H_2O Photolysis and Laser-Induced Fluorescence of OH," *Optics Letters*, Vol. 14, No. 10, 1989, pp. 473–475.

[3]Miles, R. B., and Lempert, W. R., "Quantitative Flow Visualization in Unseeded Flows," *Annual Review of Fluid Mechanics*, Vol. 29, 1997, pp. 285–326.

[4]Pitz, R. W., Brown, T. M., Nandula, S. P., Skaggs, P. A., DeBarber, P. A., Brown, M. S., and Segall, J., "Unseeded Velocity Measurement by Ozone Tagging Velocimetry," *Optics Letters*, Vol. 21, No. 10, 1996, pp. 755–757.

[5]Lewis, B. R., Berzins, L., Carver, J. H., and Gibson, S. T., "Rotational Variation of Predissociation Linewidth in the Schumann–Runge Bands of $^{16}O_2$," *Journal of Quantitative Spectroscopy and Radiative Transfer*, Vol. 36, No. 3, 1986, pp. 187–207.

[6]Cheung, A. S.-C., Mok, D. K.-W., Sun, Y., and Freeman, D. E., "The Potential Energy Curve for the $B\,^3\Sigma_u^-$ State of Oxygen and Accurate Franck–Condon Factors for the Schumann–Runge Bands," *Journal of Molecular Spectroscopy*, Vol. 163, No. 1, 1994, pp. 9–18.

[7]Freisinger, B., Kogelschatz, U., Schäfer, J. H., Uhlenbusch, J., and Viöl, W., "Ozone Production in Oxygen by Means of F_2-Laser Irradiation at $\lambda = 157.6$ nm," *Applied Physics B*, Vol. 49, No. 1, 1989, pp. 121–129.

[8]Finlayson-Pitts, B. J., and Pitts, J. R., Jr., *Atmospheric Chemistry: Fundamentals and Experimental Techniques*, Wiley-Interscience, New York, 1986, pp. 522–526.

[9]Greenblatt, G. D., and Wiesenfeld, J. R., "Time-Resolved Resonance Fluorescence Studies of $O(^1D_2)$ Yields in the Photodissociation of O_3 at 248 nm and 308 nm," *Journal of Chemical Physics*, Vol. 78, No. 8, 1983, pp. 4924–4928.

[10]Park, H., and Slanger, T. G., "$O_2(X, v = 8\text{-}22)$ 300 K Quenching Rate Coefficients for O_2 and N_2, and $O_2(X)$ Vibrational Distribution from 248 nm O_3 Photodissociation," *Journal of Chemical Physics*, Vol. 100, No. 1, 1994, pp. 287–300.

[11]Andresen, P., Bath, A., Gröger, W., Lülf, H. W., Meijer, G., and ter Meulen, J. J., "Laser-Induced Fluorescence with Tunable Excimer Lasers as a Possible Method for Instantaneous Temperature Field Measurements at High Pressures: Checks with an Atmospheric Flame," *Applied Optics*, Vol. 27, No. 2, 1988, pp. 365–378.

[12]Julienne, P. S., "$^3\Sigma_u^-$-$^3\Sigma_u^+$ Coupling in the $O_2\,B\,^3\Sigma_u^-$ Predissociation," *Journal of Molecular Spectroscopy*, Vol. 63, No. 1, 1976, pp. 60–79.

[13]Grinstead, J. H., "Temperature Measurement in High-Temperature Gases Using KrF Laser-Induced O_2 Fluorescence," Ph.D. Dissertation, Mechanical and Aerospace Engineering Dept., Univ. of Virginia, Charlottesville, VA, Jan. 1995.

[14]Waller, J. G., and McTurk, G., "Storage of Compressed Gaseous Ozone," *Journal of Applied Chemistry*, Vol. 15, No. 8, 1965, pp. 363–366.

[15]Lutz, A. E., Kee, R. J., and Miller, J. A., "SENKIN: A Fortran Program for Predicting Homogeneous Gas-Phase Chemical Kinetics with Sensitivity Analysis," Sandia National Labs., Sandia Rept. SAND87-8248, Livermore, CA, Feb. 1988.

[16]Wehrmeyer, J. A., Ribarov, L. A., Batliwala, F., Oguss, D. A., Pitz, R. W., and DeBarber, P. A., "Flow Tagging Velocimetry for Low and High Temperature Flowfields," AIAA Paper 99-0646, Jan. 1999.

[17]Lee, M. P., "Temperature Measurements in Gases Using Planar Laser-Induced Fluorescence Imaging of NO and O_2," Ph.D. Dissertation, Mechanical Engineering Dept., Stanford Univ., Stanford, CA, Nov. 1991.

[18]Axworthy, A. E., Jr., and Benson, S. W., "Mechanism of Gas Phase Decomposition of Ozone. Thermal and Photochemical Reactions," *Ozone Chemistry and Technology*, No. 21, Advances in Chemistry Series, American Chemical Society, Washington, DC, 1959, pp. 388–397.

[19]McKenzie, R. L., "Rayleigh Rejection Filters for 193-nm ArF Laser Raman Spectroscopy," *Optics Letters*, Vol. 18, No. 12, 1993, pp. 995–997.

[20]Miles, R., Lempert, W., and Zhang, B., "Turbulent Structure Measurements by RELIEF Flow Tagging," *Fluid Dynamics Research*, Vol. 8, No. 1, 1991, pp. 9–17.

R. P. Lucht
Associate Editor